X-ray diffraction and micro-Raman spectroscopy analysis of new nickel hydroxide obtained by electrodialysis

S. Deabate [a], F. Fourgeot [a,b], F. Henn [a, *]

[a] *Laboratoire de Physicochimie de la Matière Condensée, CC003, UMR 5617, Université Montpellier II, URA CNRS D047, Place Eugène Bataillon F-34095, Montpellier Cedex 05, France*
[b] *RBC, 89 Boulevard Alsace Lorraine, 93110 Rosny sous Bois, France*

Abstract

Industrial nickel hydroxide samples produced by electrodialysis have been characterized both by X-ray diffraction (XRD) and by micro-Raman spectroscopy. A comparison with some commercial products of β-type $Ni(OH)_2$ is made. Aged in KOH solution, these nickel hydroxides are transformed to the β-$Ni(OH)_2$ phase and undergo Ostwald ripening, leading to crystallite sizes ranging between 260 and 380 Å with a reduction in defects. The anisotropic broadening of the XRD peaks in the β-$Ni(OH)_2$ pattern is interpreted in terms of crystalline lattice micro-strains and crystallite size. For the first time, Rietveld refinement has been performed on industrial $Ni(OH)_2$. The results indicate that the micro-strain effects increase the peak width according to the sequence of families $(hk0) \rightarrow (00l) \rightarrow (h0l)$. This study shows that the presence of proton vacancies leads to a lower degree of distortion in the crystalline lattice than does the presence of stacking faults or the adsorption of inorganic species at the border of the crystallites. A very high concentration of point defects inducing strong distortions in the crystal lattice is correlated with the presence of high energy Ni–O bond vibrations in the Raman spectra, with a frequency shift towards unusually high values. © 2000 Elsevier Science S.A. All rights reserved.

1. Introduction

Ni–MH is one of the most promising battery systems for electric and hybrid vehicle propulsion in the mid-term. Substitution of Cd in alkaline batteries by metal hydrides results in a higher specific capacity, and present efforts world-wide to improve the high performance of metal hydride electrodes make imperative the development of new active materials and electrode designs for positive nickel electrodes with improved capacity and high power density. For this reason, irregularly shaped nickel hydroxide with high tap density (> 1.8 g/cm^3) and doped with metallic cations (Co, Zn,...) has been developed. This high-density nickel hydroxide is obtained via a new electrochemical route, namely by an electrodialytic process. The electrodialysis cell is made of an anodic compartment where Ni^{2+} cations are produced by electrodissolution of nickel metal, separated from the cathodic compartment containing OH^- anions by an anionic membrane. When direct current is applied, this membrane allows OH^- anions to migrate selectively from the cathodic to the anodic compartment, leading to the precipitation of $Ni(OH)_2$ onto the membrane at the anodic side. The $Ni(OH)_2$ is removed from the surface of the anionic membrane and smoothly crushed to obtain a fine powder (mean size diameter $\emptyset = 100$–200 μm) [1].

X-ray diffraction (XRD) and vibrational spectroscopy (Raman and infrared) measurements were performed in order to obtain information about the crystallographic structure and the nature of the Ni–O and O–H bonds, respectively. The chemical composition of the different compounds was determined by energy dispersive spectroscopy, and by chemical and thermogravimetric analyses.

It is well known that the crystallographic state and the morphology of nickel hydroxide have significant influences on its electrochemical behaviour [2–5]. The peak broadening of the β-$Ni(OH)_2$ XRD patterns has often been

* Corresponding author. Tel.: +33-467-14-48-55; fax: +33-467-144-290; e-mail: fegh@lpmc.univ-montp2.fr

correlated with the electrochemical efficiency by Sherrer's formula for evaluation of crystallite size [6–9]. Terasaka et al. [7] linked the electrochemical efficiency to the width of the (101) peak, and Watanabe et al. [8] to that of the (001) and the (101) peaks since Bernard et al. indicated that peaks (10l) are especially broadened when the hydroxide is more reactive [10].

Nevertheless, the broadening of the diffraction peaks exhibits an anisotropic behaviour with a distinction between the indices h, k and the index l, which leads to quite narrow ($hk0$) lines, while the (001) and (10l) lines are more broadened. Barnard et al. claimed that the selective broadening is consistent with misalignment along the basal plane of a laminar structure [9]. More recently, Delmas and Tessier proposed a suitable interpretation based on the presence of stacking faults randomly distributed within the oxygen hexagonal compact packing, leading to the existence of some face-centred cubic domains [11].

We have studied the broadening of the β-Ni(OH)$_2$ XRD peaks of a typical non-doped nickel hydroxide Ni(OH)$_2$ synthesized by electrodialysis [1] and of some commercially available materials that were used as references. We consider that the diffraction lines are the convolution of some position and intensity parameters, which depend on the one hand on the contribution of the sample morphology, that is, the crystallite size, and on the other hand, on the existence of micro-strain in the lattice due to the presence of stacking defects, adsorption of inorganic species (water and anions) and proton vacancies. These parameters influence the intensity around the Bragg (2θ) position, that is to say, the form profile of the diffraction peak. The XRD data of different β-Ni(OH)$_2$ samples were

firstly analysed by a peak-by-peak approach using the Sherrer and Warren–Averbach formulae, then in an overall way by the Rietveld refinement method. Raman and IR spectroscopy data are also reported, in order to complete the XRD study.

2. Sample characterization

Five different nickel hydroxide samples were examined. The commercially available A–B samples (supplied by Aldrich Chemical Company and Tanaka Chemical Corporation, respectively) have spherical morphology. The C sample is an industrial product (EMISA, Spain) obtained by precipitation, while the D–E samples were synthesized by electrodialysis [1]. The latter three samples do not show a spherical morphology. Compound B contains small quantities of Cd and Co as dopant and compound C contains only Co (see Table 1). The A and B materials show typical XRD patterns of β(II)-Ni(OH)$_2$ with a poor degree of crystallization. The other ones exhibit an even poorer crystalline state (Fig. 1). A recrystallization after 5 days of ageing in KOH (5N) solution was performed in order to recover a better-crystallized β(II)-phase, especially for the D and E samples. The cell parameters of the β(II)-phases (Table 1) are close to those published in the literature [Refs. [2,3] and references therein]. The c parameter, however, is slightly larger than 4.593(1) Å, the value refined by Greaves and Thomas for a well-crystallized β-Ni(OH)$_2$ and reported by Delahaye-Vidal et al. [3], suggesting an increase of the inter-sheet distance, and which probably correlates with a small quantity of protonic defect.

Table 1

Approximate chemical composition of the nickel hydroxides A–E and cell parameters of the corresponding β-Ni(OH)$_2$ phases (space group: P$\bar{3}$m1). Samples noted with a star were aged in 5N KOH solution for 5 days at room temperature. In samples D and E, the c parameters were evaluated from decomposition of the diffractograms in the β- and α-phases

Chemical analysis data

	"As-received" sample		Sample after ageing in KOH solution
A	Ni(OH)$_2$, 0.03H$_2$O	A*	Ni(OH)$_2$, 0.03 H$_2$O
B	Ni$_{0.95}$Co$_{0.01}$Cd$_{0.04}$(OH)$_2$, 0.025H$_2$O	B*	Ni$_{0.95}$Co$_{0.01}$Cd$_{0.04}$(OH)$_2$, 0.025H$_2$O
C	Ni$_{0.98}$Co$_{0.02}$(CO$_3$)$_y$(SO$_4$)$_{0.03}$(OH)$_{1.96-2y}$, 0.15H$_2$O	C*	Ni$_{0.98}$Co$_{0.02}$(CO$_3$)$_y$(OH)$_{2-2y}$, 0.15H$_2$O
D	Ni(CO$_3$)$_y$(SO$_4$)$_{0.09}$(OH)$_{1.82-2y}$, 0.65H$_2$O	D*	Ni(CO$_3$)$_y$(OK)$_{0.03}$(OH)$_{1.97-2y}$, 0.5H$_2$O
E	Ni(CO$_3$)$_y$(SO$_4$)$_{0.15}$(OH)$_{1.7-2y}$, 0.7H$_2$O	E*	Ni(CO$_3$)$_y$(OK)$_{0.03}$(OH)$_{1.97-2y}$, 0.5H$_2$O

Crystallographic data

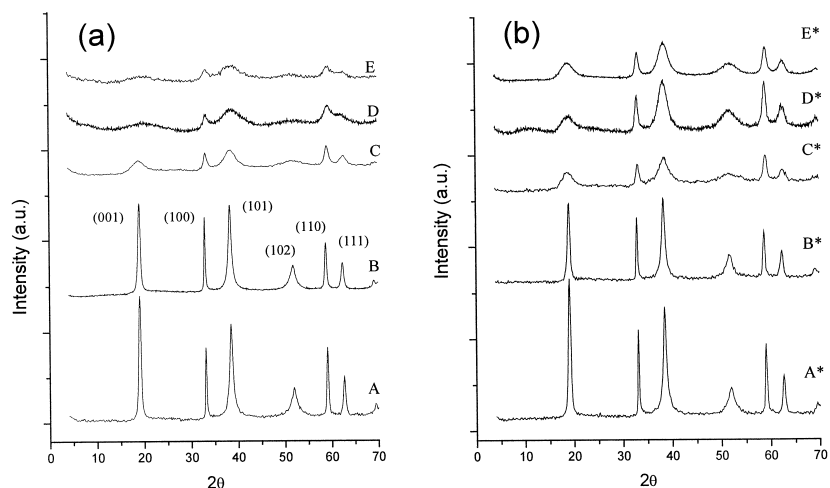|	β-type			In KOH → β-type	
	a (Å)	c (Å)		a (Å)	c (Å)
A	3.128(3)	4.635(3)	A*	3.123(2)	4.647(2)
B	3.136(1)	4.637(1)	B*	3.137(1)	4.654(1)
C	3.120(3)	4.660(3)	C*	3.123(6)	4.640(6)
D	3.12(2)	4.61(4)	D*	3.120(2)	4.667(2)
E	3.12(2)	4.63(3)	E*	3.118(1)	4.645(2)

Fig. 1. (a) XRD diagrams of samples A–E, (b) after ageing in KOH (5N) solution for 5 days at room temperature.

In order to obtain their chemical composition, all the samples were analysed by thermal gravimetric analysis, energy dispersive spectrometry and atomic absorption spectrophotometry. The combination of these different experimental techniques allowed us to obtain the chemical formulae reported in Table 1. Nor were we able to measure the carbonate content in the C–E and C*–E* samples, although the presence of traces of CO_3^{2-} anions was clearly shown by infrared spectroscopy.

XRD analysis was carried out with a Seifert θ–θ goniometer, using a Cu anticathode $K_{\alpha 1}$–$K_{\alpha 2}$ radiation (the diffractograms, reported in 2θ scale, were recorded with a step of 0.05° and a counting time of 10 s. For those employed in the Rietveld refinement, the following acquisition conditions were used: 0.02° step and 20 s counting time).

The X-ray patterns of samples B* and E* were refined with the Rietveld technique using the FULLPROF Refinement Program (PC version: 2.6.1, Oct94-JRC).

All samples were analysed by confocal micro-Raman spectroscopy, a particularly efficient technique for studying morphologically and structurally heterogeneous materials. Several spectra were recorded for each sample and the more representative ones are discussed in Section 3.2. Raman spectra were recorded via a Labram spectrometer coupled to a 13 × 40 Olympus microscope, equipped with a 100 × objective. The source was a He–Ne laser emitting a 632.8 nm excitation line, whose power did not exceed 10 mW on the sample. It has been verified that, in these experimental conditions, no structural modifications were induced in the samples by local heating.

Infrared spectra were obtained using an IRTF BOMEM DA8 spectrophotometer with a global source and an MCT detector cooled by liquid nitrogen. The powder samples were mixed with KBr and pelletized prior to being analysed.

3. Results and discussion

3.1. X-ray diffraction

3.1.1. Broadening due to crystallite size effects: the Scherrer formula

The broadening of the diffraction bands can be ascribed to the effect of the finite size of the coherent diffraction fields. The Scherrer formula [12] makes possible the evaluation of the crystallites' size according to the direction $[hkl]$ by the expression:

$$T = \lambda K / [H \cos(\theta)] \qquad (1)$$

T is the crystallite size, λ is the wavelength of the incident X-ray radiation ($\lambda = 1.54$ Å), K is the Scherrer constant (kept in this work equal to 1), θ is the Bragg angle for the direction $[hkl]$. H (expressed in radians) is defined as $H = (\nu^2 - \nu_O^2)^{1/2}$, where ν is the experimental width at half height of the diffraction peak and ν_O is the instrumental angular widening determined from the diffractogram of a 325-mesh (44 μm) silicon powder, recorded under the same acquisition conditions as for the nickel hydroxide.

According to the SEM pictures (Fig. 2), the crystallites are comparable to hexagonal plates of diameter **d** and thickness **e** (see Table 2). The particle size calculated from the width of the (110) peak corresponds roughly to the diameter **d**, while that calculated from the width of the (001) peak corresponds to the thickness **e**. The results of the calculations made by the Scherrer formula are reported in Table 2. Compounds A and B are characterized by larger crystallites compared with the crystallites obtained by electrodialysis (compounds D and E), while sample C exhibits an intermediate behaviour. After ageing in KOH (5N) solution for 5 days, it is worth noting a decrease of the crystallite size for compounds A and B, while compounds D and E show an increase of their crystallites' size. The **d** sizes of crystallites seem to converge to a particular
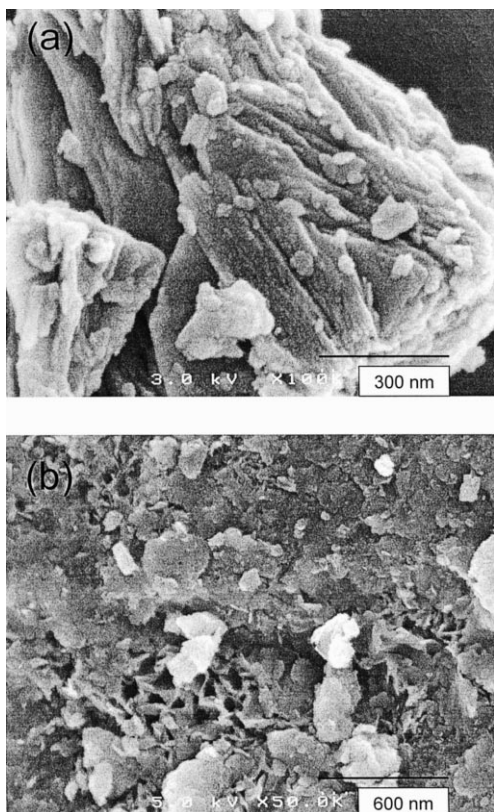
Fig. 2. SEM image of (a) crystallites of sample B; (b) crystallites of sample D.

range between 260 and 380 Å. Samples D and E undergo an Ostwald ripening, which is a typical dissolution/re-crystallization growth process tending to minimize the grain surface [3]. The crystallites then grow to a critical size, probably with values ranging between 260 and 380 Å. It is nevertheless surprising to note a change for compounds A and B.

Table 2
Crystallite sizes (CS) calculated from the Scherrer formula and micro-distortion degrees (MD) ε_a, ε_c calculated from the Warren–Averbach formula according to a and c

Sample	CS						MD	
	001, e (Å)	100 (Å)	101 (Å)	102 (Å)	110, d (Å)	111 (Å)	ε_a	ε_c
"As-received" sample								
A	370	805	235	130	595	385	0.1	0.3
B	350	1130	250	140	515	340	0.1	0.3
C	70	260	80	40	230	155	0.2	1.4
D	16	110	24	14	85	30	1.0	5.5
E	13	90	15	17	60	35	1.1	6.3
Sample after ageing in KOH solution								
A*	345	950	245	120	560	385	0.1	0.3
B*	310	890	250	140	385	280	0.1	0.4
C*	75	265	85	40	260	150	0.2	1.3
D*	24	136	43	26	126	67	0.5	3.5
E*	25	115	37	22	110	69	0.5	3.5

Further to this simple peak analysis, the values obtained show great disparities according to the different directions [hkl]. For all the compounds, the biggest sizes are calculated for the (100) and (110) peaks, in agreement with the electronic images showing crystallites of plate type shape. The thickness **e** is always less than the diameters of the plates. The (101), (102) and (111) peaks lead to smaller calculated sizes when the value of the index l is higher. This is in agreement with the conclusions reported by Bernard et al. [10]. Also, the broadening of the diffraction peaks exhibits anisotropic behaviour with a distinction between the indices h, k and the index l, leading to incoherent results for the crystallite size. The greater broadening associated with the index l suggests the presence of micro-distortions, particularly in the inter-layer space due to some stacking faults as recently proposed by Delmas and Tessier [11], to protonic vacancies, as well as to the adsorption of inorganic species at the border of the crystallite. We propose to describe these defects by a phenomenological model of micro-strain.

3.1.2. Broadening due to micro-strain effects: the Warren–Averbach formula

The presence of micro-distortions induces both isotropic and anisotropic broadening of the Bragg reflections. The micro-distortions are local variations of the reticular distances ($M_{hkl} = 1/d_{hkl}^2$), produced by non-uniform crystalline distortions. They are generated by crystalline defects, such as stacking faults, vacancies or insertions, as well as by local variations of the chemical composition. A simple way to understand this effect is to consider that the presence of micro-distortions is equivalent to the existence of micro-strain, which involves a distribution of the $M_{hkl} = 1/d_{hkl}^2$ variables. Let us consider the presence of vacancies in a cubic lattice that involves a space fluctuation of the cell parameter a. Taking into account cubic symmetry, this leads to an isotropic broadening of the diffraction peaks. One can define the distortion parameter $\varepsilon = \delta\mathbf{d}/\mathbf{d}$ (Fig. 3). By differentiating the Bragg law, one obtains the angular dispersion of intensity $\Delta(2\theta) = 4\varepsilon \tan(\theta)$. By

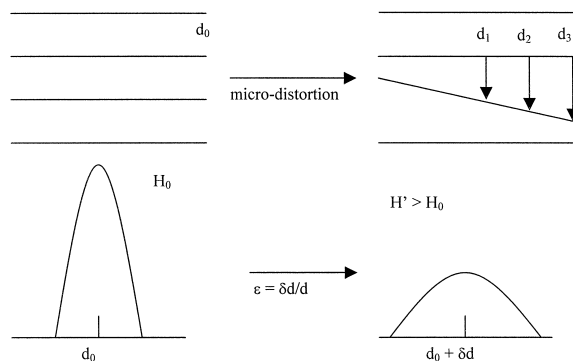Fig. 3. Schematic illustration of micro-strain and its effects on the diffraction peak profile; d is the reticular distance; H is the half-height width of the diffraction peak; ε is the distortion parameter.
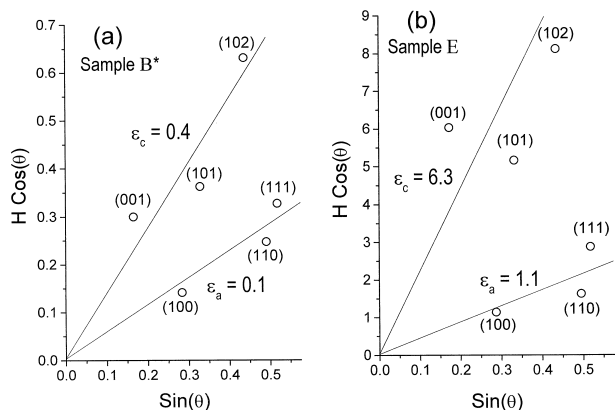
Fig. 4. Layout of the Warren–Averbach relation for: (a) sample B* and (b) sample E. B* is a ''well crystallized'' compound, whereas E presents a very poorly crystallized structure.

Fig. 5. Rietveld refinement of B* XRD.

introducing this result into the Scherrer formula (Eq. (1)), the Warren–Averbach relation [13] is obtained:

$$H \cos (\theta) = \lambda/T + 4\langle \varepsilon^2 \rangle^{1/2} \sin (\theta) \qquad (2)$$

where $\langle \varepsilon^2 \rangle^{1/2}$ is the mean-square-root of the deformation. From the Warren–Averbach relation, it is necessary to plot $H \cos (\theta)$ against $\sin (\theta)$ to directly obtain the micro-distortion degree $\langle \varepsilon^2 \rangle^{1/2}$ and the average crystallite size. The results obtained on samples B* and E are illustrated in Fig. 4 and show that one can distinguish two families of peaks, depending on the Miller indices. The deformation degree is larger for peaks described by the index l. One can define a deformation degree ε_c associated with the index l and a deformation degree ε_a related to the indices h, k. The (101) and (111) peaks are in an intermediate situation since they are the convolution of these two deformation degrees. On the other hand, the average size of crystallites, 60 and 400 Å, respectively, for compounds E and B*, deduced from the Warren–Averbach approximation, is within the order of magnitude calculated by Scherrer's formula. The parameters ε_a and ε_c are reported in Table 2. The effect of micro-strain increases when the crystallite size decreases. That is to say, it increases according to the sample sequence $A \rightarrow E$ and $A^* \rightarrow E^*$. After ageing in KOH, the micro-distortion degrees decrease in compounds D* and E*, while there is no significant change for the other compounds. The presence of larger deformations in the electrodialysis compounds can be related to their smaller crystallite size and to the phase transformation that takes place when they are aged in KOH. Furthermore, the smaller the crystallite size, the greater is the effect of the adsorption of molecular species onto the crystallite edges, which creates perturbations inside the crystal lattice.

3.1.3. Rietveld refinement

In addition to the effects of crystallite size, we introduced the effects of micro-strain to interpret the broadening of the diff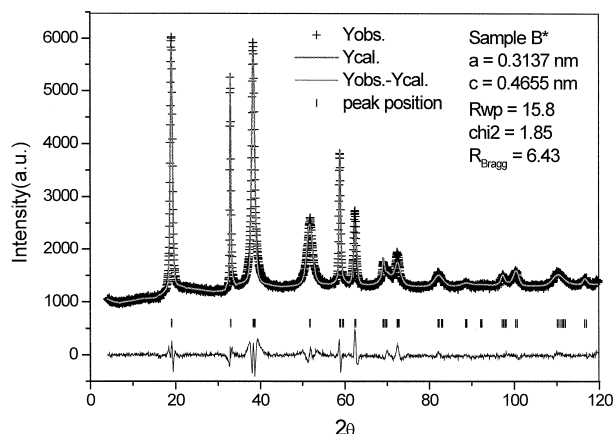raction peaks. In order to confirm our interpretation, we attempted to refine the XRD of compounds B* and E* by the Rietveld method using the FULLPROF program (Figs. 5 and 6). See Appendix A for more details about the Rietveld method used in this investigation.

The value of the Bragg coherence factor is 6.4% for the B* sample, showing that it is possible to interpret the peak broadening by micro-strain and size effects. Sample E* shows a diffraction diagram with broader bands, resulting from a poorer crystallization state with a more important role for micro-strain. Consequently, the refinement is more difficult and the Bragg factor is higher: 10.2%. However, the values of the thermal agitation factors are still positive (see Table 5, Appendix A). This reinforces the validity of the refinement of peak broadening by the micro-strain model. Moreover, the occupancy rates show the presence of protonic and OH$^-$ vacancies [3,10]. In all cases, the constraint parameter ι related to the index l is higher than the parameter α depending on the indices h, k (see Table 5a and b, Appendix A). In fact, the micro-strain effects increase the peak width according to the sequence of families $(hk0) \rightarrow (00l) \rightarrow (h0l)$. The Rietveld refinement
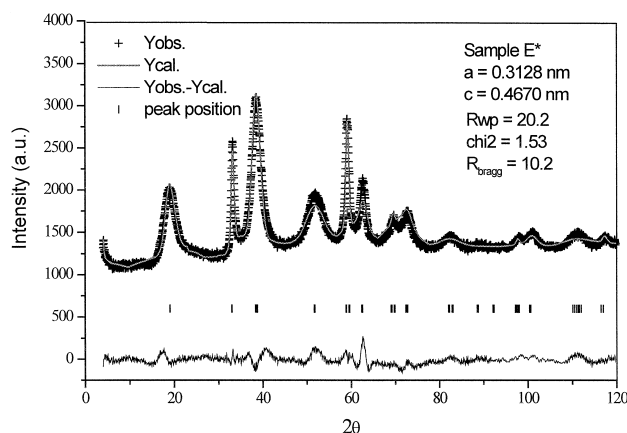

Fig. 6. Rietveld refinement of E* XRD.

of samples E* and B* shows that the size effects mainly depend on the set of indices ($00l$) for the first sample, while they are greater for the set of indices ($h0l$) in the case of the second sample. In conclusion, the presence of micro-strain in the crystal lattice, due especially to micro-strain generated in the inter-layer space, in association with the size effect of the diffraction fields, seems to correctly reflect the broadening of the Bragg peaks. As in the peak-by-peak approach, the micro-strain shows anisotropic behaviour, with strong deformations associated with the index l.

3.2. Raman and IR spectroscopy experiments

3.2.1. Raman spectroscopy experiments

Samples A–E (Figs. 7 and 8) show very dissimilar Raman spectra because of their different morphology and structural characteristics. Compounds A–B exhibit typical nickel hydroxide spherical particle spectra (Fig. 7) [14]. These samples can be considered as β-Ni(OH)$_2$ containing some structural defects (see Table 3) and so-called ''badly crystallized β'' [10,11,14,16–21]. The spectrum of sample C, Fig. 7, is also typical of β_{bc}-Ni(OH)$_2$, but shows some additional features, namely the enhanced intensity of the peak located around 520 cm^{-1} and the presence of a shoulder at higher wavenumbers. In order to explain all its Raman lines, one has to take into account the presence in sample C of some α-Ni(OH)$_2$ (see Fig. 7c and Table 3)

[20–22], which was not detected by XRD. The peak located at 515–517 cm^{-1} in the spectra of compounds B–C has to be correlated with the presence of doping agents such as Co and Cd [10,21,23]. It has been demonstrated that Co is substituted for Ni in the lattice and that its oxidation state is often higher than that of nickel [10,21]. Some protonic vacancies are consequently induced in the nickel hydroxide lattice to balance the overall charge of the material. The spectra of the electrodialysis samples D and E are similar to each other and show some unique features (Fig. 8, Table 3). Firstly, no protonic vacancies are observed, in agreement with the smaller cell parameter c determined by XRD analysis. Worth noting, the wavenumber of the Ni–O(H) stretching vibration, located around 465 cm^{-1}, is unusually high for a β-type material. In order to explain the D–E Raman data, the hypothesis of a non-close-packed β-form of Ni(OH)$_2$, such as that proposed by Cornilsen et al. [20,21] for the discharged ''active mass'' (e.g., electrochemically cycled), has to be rejected because of the lack of any Raman line around 530 cm^{-1}. The spectra reported in Fig. 8 also show qualitative agreement with the ''α-chemical'' type patterns observed by several authors [20–22], but the hypothesis of a compound entirely constituted of α-phase is in sharp contrast with the X-ray study. Moreover, in the OH stretching frequency region, it is still possible to distinguish the peaks due to the surface and bulk OH groups (Fig. 8b, Table 3), when normally the chemically precipitated α-Ni(OH)$_2$ shows only one very broad band centred around 3600
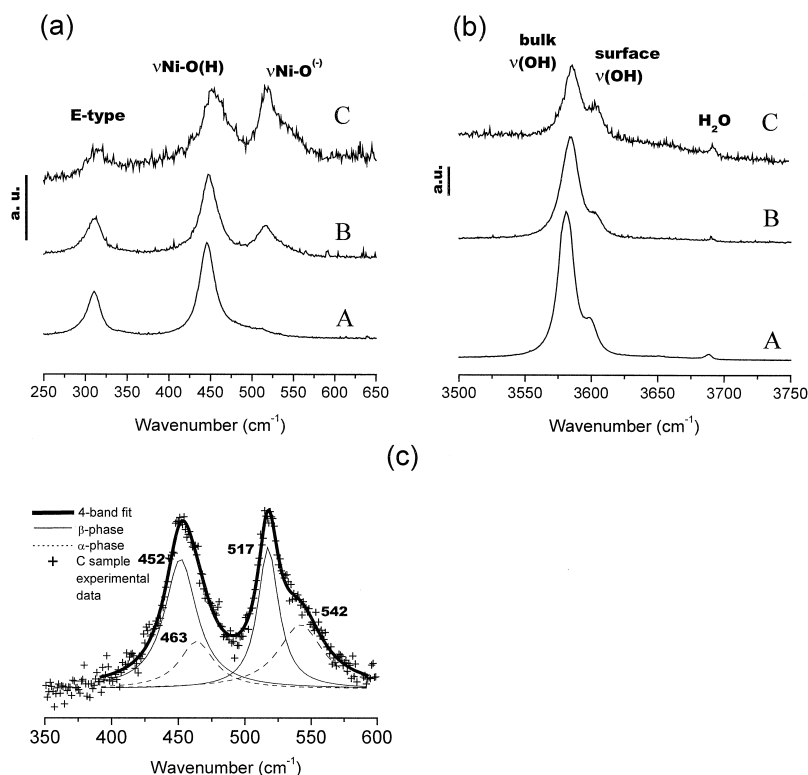

Fig. 7. Raman spectra of samples A–C: (a) frequency region of Ni–O lattice vibrational modes; (b) OH group stretching vibrations; (c) four-band fit of the nickel–oxygen bond frequency region of sample C.
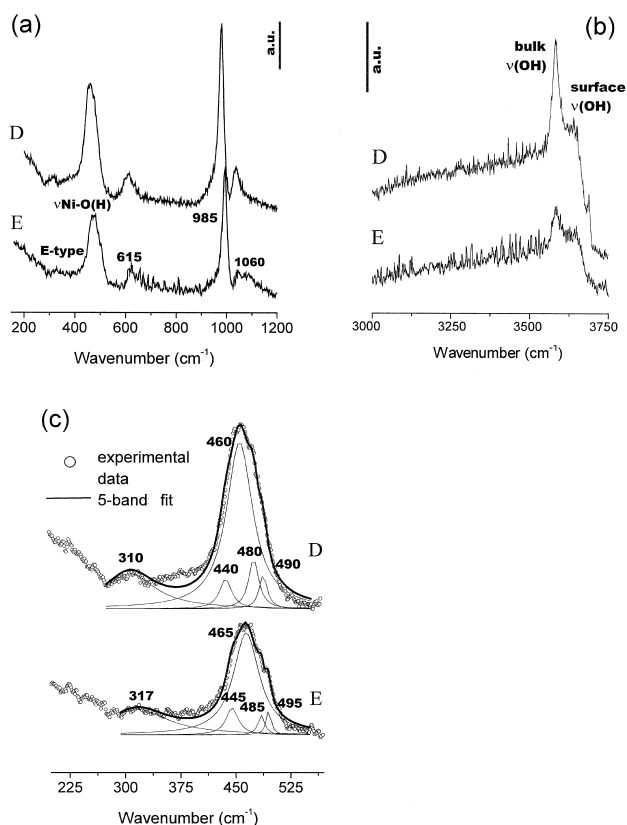
Fig. 8. Raman spectra of samples D–E: (a) frequency region of Ni–O lattice vibrational modes; (b) OH group stretching vibrations; (c) five-band fit of nickel–oxygen bond frequency region (a band around 380 cm^{-1} is likely to be present, but is not taken into account).

cm^{-1} [20–22]. A fit of the Ni–O peak in samples D and E was attempted in order to gain deeper insight into the structure and to discriminate the different contributions of the co-precipitated β- and α-phases. One of the simpler solutions is displayed in Fig. 8c. Reproducible data for both samples confirm the noticeable presence of a peak located at 460–465 cm^{-1} next to a peak at 440–445 cm^{-1}, which can be ascribed to ''well crystallized'' β-Ni(OH)$_2$. After the fit and according to the X-ray data, we are forced to identify the principal band at 460–465 cm^{-1} as the Ni–O(H) stretching vibration of a highly defective β-Ni(OH)$_2$, denoted β$_{hd}$-Ni(OH)$_2$, which constitutes the untreated samples D and E. The unusually high frequency is likely to be correlated with the high value of micro-strains established by the XRD study (Table 2). The higher degree of disorder is demonstrated also by the pronounced broadening of the band at 310–317 cm^{-1} in the D–E Raman spectra.

A substantial contribution to the crystalline distortion effects is certainly given by some adsorbed sulphate species, whose presence is indicated by a complex system of bands located in the 600–1100 cm^{-1} range (Fig. 8a). The two peaks at 1060 and 985 cm^{-1} have been observed in aqueous H$_2$SO$_4$ solution and correspond, respectively, to the hydrogen sulphate HSO$_4^-$ and sulphate SO$_4^{2-}$ ion bands [see, for example, Ref. [24]]. The band at 615 cm^{-1} is distinctive of the heptahydrated NiSO$_4$, which also exhibits bands around 470, 440 and 380 cm^{-1} [25]. These bands could explain some of the unique features revealed by the fits shown in Fig. 8c, namely some of the weak peaks located at higher wave numbers.
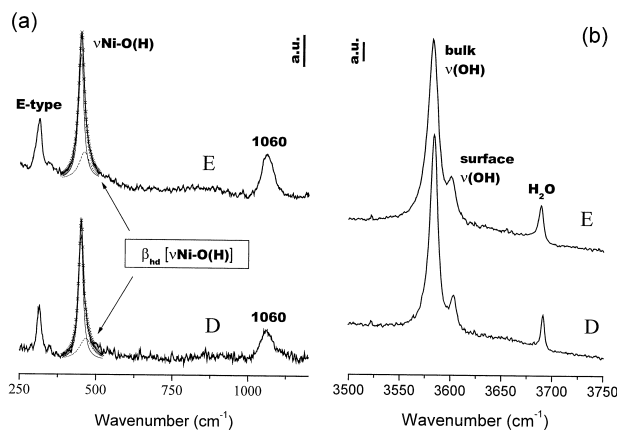
Table 3

Raman band positions (cm^{-1}): E-type = E-type vibration of the Ni–OH lattice; νNi–O(H) = Ni–O stretching vibration of Ni^{2+} species associated with OH$^-$ groups; νNi–O$^{(-)}$ = Ni–O stretching vibration of Ni^{2+} species associated with O^{2-} (proton vacancy sites [10]); bulk νOH = symmetric stretch of the hydroxide groups of the crystalline bulk; surface νOH = symmetric stretch of the hydroxide groups located at the crystallites' surface; H$_2$O = O–H stretching vibration of water molecules physisorbed onto the nickel hydroxide particles

Sample	Ni(OH)$_2$ peak position									
	E-type	νNi–O(H)			νNi–O$^{(-)a}$			Bulk νOH	Surface νOH^a	H$_2$O
		β-type	β$_{hd}$-type	α-type	β-type	β$_{hd}$-type	α-type			
''As-received'' sample										
A	310	445	–	–	510^b	–	–	3580	3600	3690
B	310	445	–	–	515	–	–	3585	3600	3690
C	315	452	–	463	517	–	542	3585	3600	3690
D	310	440	460	–	–	480^c, 490^c	–	3590	3640	–
E	317	445	465	–	–	485^c, 495^c	–	3585	3640	–
Sample after ageing in KOH										
A*	310	445	–	–	∼ 500^b	–	–	3580	3595	3685
B*	304	440	–	–	510	–	–	3580	3595	3685
C*	315	448	–	460	515	–	545	3585	3600	3690
D*	315	451	467	–	–	–	–	3583	3603	3690
E*	313	447	460	–	–	–	–	3582	3600	3690

^{a}Raman lines attributable to ''structural defects'': they are not predicted by the model first proposed by Mitra [15] for a well-crystallized β-Ni(OH)$_2$.
^{b}Very weak band.
^{c}Uncertain assignment.

Fig. 9. Raman spectra of samples D* –E*: (a) frequency region of Ni–O lattice vibrational modes; (b) OH group stretching vibrations.

Raman spectra were collected after ageing samples (A*–E*) in KOH. No significant changes in the A*–C* materials were observed in comparison with the untreated samples (spectra not reported), in accordance with the small variations in the degree of micro-distortion. The proportion of α-Ni(OH)$_2$ contained in the C sample also seems to be only slightly lowered after KOH ageing, probably due to the stabilizing effect of the dopants. In contrast, the D*–E* spectra are close to the typical β$_{bc}$-Ni(OH)$_2$ ones (Fig. 9), in agreement with the re-crystallization phenomenon observed by XRD and the lowering of the micro-distortion values (Table 2). A shoulder is noted, however, towards high wave numbers (460–467 cm^{-1}) in the Ni–O(H) stretching vibration band centred at 447–451 cm^{-1} for compounds E* and D*, respectively (see the two-band fit in Fig. 9a). This shoulder can be assigned to the β$_{hd}$-Ni(OH)$_2$ still present after KOH treatment, in agreement with the high amount of residual distortion measured in the aged compounds. It is worth noting that most of the sulphate present has been removed (also confirmed by IR analysis, see Section 3.2.2) — only the band due to the HSO$_4^-$ is still observed.

3.2.2. IR spectroscopy experiments

In order to confirm our hypothesis about the β$_{hd}$-Ni(OH)$_2$ nature of compounds D–E, we have also investigated the IR spectra of these samples. Fig. 10 shows the IR data of samples C–E, that is, the samples containing a higher degree of micro-strain according to XRD. In the high wave number region, the spectra exhibit a narrow band located around 3645 cm^{-1}, due to the ν(OH) stretching vibration of the hydroxide groups of Ni(OH)$_2$ sheets not involved in interactions (''free'' OH). The broad band centred around 3400 cm^{-1} is due to the ν(OH) mode of the hydroxide groups involved in hydrogen bonding, both from the Ni(OH)$_2$ sheets (OH$^-$ groups interacting with adsorbed species, particularly H$_2$O) and from adsorbed H$_2$O [26–28]. The presence of the sharp peak due to ''free'' OH groups confirms the β-nature of the com-

pounds. The non-negligible intensity of the 3400 cm^{-1} peak is in accordance with the low degree of crystallization and the small crystallite size of the samples [3,5]. The peaks around 1630 and 520 cm^{-1} are due to bending vibration of water molecules adsorbed onto the Ni(OH)$_2$ by hydrogen bonding, and of the hydroxyl groups of the Ni(OH)$_2$, respectively [3,5]. The complex system of absorptions located in the 1600–500 cm^{-1} range demonstrates also the presence of inorganic anions weakly bonded to the nickel ions of the sheets [29,30]. The simultaneous presence of three bands centred around 1100 cm^{-1} and of a strong absorption region located around 620 cm^{-1} reveals sulphate anions linked to the lattice by two oxygen atoms, taking the place of OH$^-$ ions [5]. The different intensity ratios between the bands in the three compounds indicate a mixture of single- and double-bonded anions (C_{3v} and C_{2v} symmetries, respectively) in variable quantities for different samples. The coupled bands centred around 1400 cm^{-1} and the two peaks located, respectively, around 800 and 680 cm^{-1} are due to the presence of small quantities of single-bonded carbonate ions of C_{2v} symmetry [Refs. [3,5] and references therein]. A weak absorption around 1000 cm^{-1}, due to the ν_1 vibration mode, is probably present, but hidden by the sulphate absorptions.

Considering the similarity between the IR spectra of samples D and E and those reported for Ni(OH)$_2$ with an interstratified structure [16–19], it is likely that small amount of α-phase is formed in the samples obtained by electrodialysis.

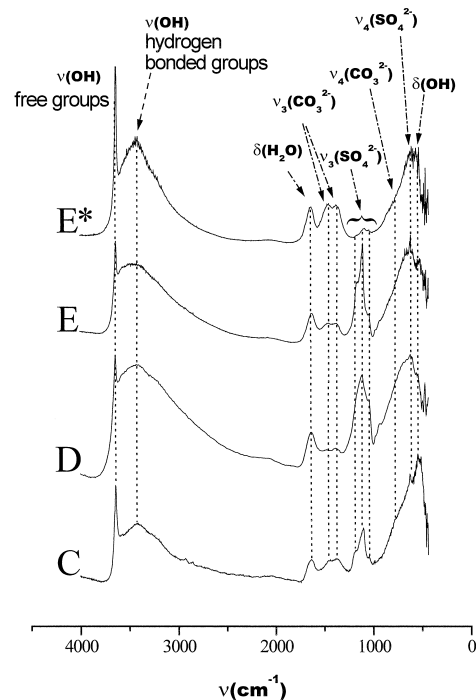After ageing, the absorptions from the sulphate species disappear almost completely and a re-crystallization phe-

Fig. 10. IR spectra of samples C–E and E*.

nomenon is displayed by the enhancement of the ''free'' OH peak. Carbonate and water are still present. A selected spectrum (sample E*) is shown in Fig. 10.

4. Correlation between X-ray and Raman data

In a qualitative way, Raman spectra reflect the degree of disorder of the sample as derived by XRD pattern analysis. Proton vacancies are likely to contribute to the crystal lattice distortion, promoting electrostatic repulsion between the $Ni(OH)_2$ sheets. They seem to especially influence the value of the c parameter of the unit cell, which increases when the quantity of protonic defects increases as does the amplitude of the corresponding Raman line. One can observe in Table 1 that sample C, the sample with the biggest intensity of the $Ni-O^{(-)}$ band relative to the $Ni-O(H)$ band, also has the largest c parameter. Similarly, samples D–E, which do not show strong Raman lines due to proton vacancies, have the smallest c values. A diagram suggesting the existence of a correlation between the crystalline cell parameter c and the intensity of the $Ni-O^{(-)}$ Raman band is reported in Fig. 11: the intercept of the linear fit line with the abscissa is at a value of 4.60 Å. In contrast, the general increase of the c parameter after ageing in KOH (Table 1, samples A*–B* and D*–E*) cannot be explained by invoking protonic defects since the corresponding $Ni-O^{(-)}$ lines remain almost unchanged (samples A*–C*) or have disappeared (samples D*–E*) in the aged compounds. On the other hand, one has to consider that in samples C–E, the degree of micro-distortion is reduced by KOH ageing, but they still have a high degree of disorder relative to the reference compounds (beta-spherical particles $Ni(OH)_2$). Therefore, sources of crystalline defects other than protonic vacancies have to be considered.

Protonic defects are the cause of a larger inter-sheet distance because of a stronger electrostatic repulsion between the adjacent slabs. Nevertheless, this kind of struc-
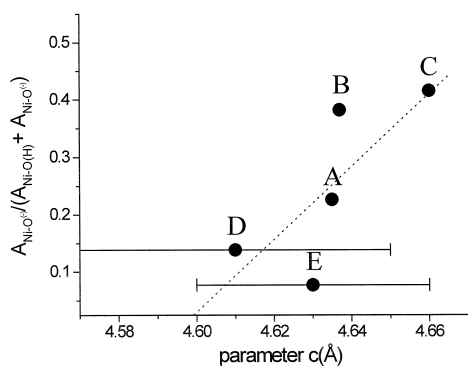

Fig. 12. Layout of Ni–O bond Raman lines as a function of micro-strains (a) ε_a and (b) ε_c. (●) Position of Ni–O(H) bond lines; (x) line position calculated as the average of all the Ni–O lattice vibrational modes according to Eq. (3); (- - -) linear fit of Ni–O(H) bond lines data.

tural defect is not likely to be solely responsible for the crystal distortion phenomenon. In Fig. 12, the positions of the Ni–O Raman bands are plotted as a function of the micro-distortion degrees calculated starting from the Warren–Averbach formula. The wave number of the Ni–O bands increases according to both ε_a and ε_c micro-strain parameters. The increase of the Ni–O lattice mode wave numbers is due to a loss in arrangement of the crystalline structure. When plotting the wave number of the Ni–O(H) bands only, data appear to be concentrated around the same straight line. However, when introducing a new arbitrary parameter defined as the average of the wave numbers of all the Raman bands in the Ni–O lattice vibrational modes domain (e.g., Raman lines due to ''badly crystallized'' and ''highly defective'', β- and α-Ni–O(H)–Ni–O$^{(-)}$ bonds) weighted by the respective amplitudes, two trends are obtained with a significant larger slope for the samples containing more protonic defects. The weighted average band position has been chosen arbitrarily to account for the occurrence of new Raman lines related to the presence of defects and is expressed as:

$$\text{Average band position} = \left[(\nu_1 A_{\nu 1}) + (\nu_2 A_{\nu 2}) + \ldots \right.$$
$$+ (\nu_n A_{\nu n}) \left] / \left[A_{\nu 1} + A_{\nu 2} \right. \right.$$
$$+ \ldots + A_{\nu n} \right] \qquad (3)$$

Fig. 11. Evolution of the amplitude ratio of the [Ni–O$^-$/(Ni–O$^-$ + Ni–OH)] Raman lines for samples A–E as a function of their c cell parameter: (- - -) is the data linear fit. Data are plotted taking into account the β-phase Raman lines only. For samples A, B and C, error bars are within the thickness of the point.
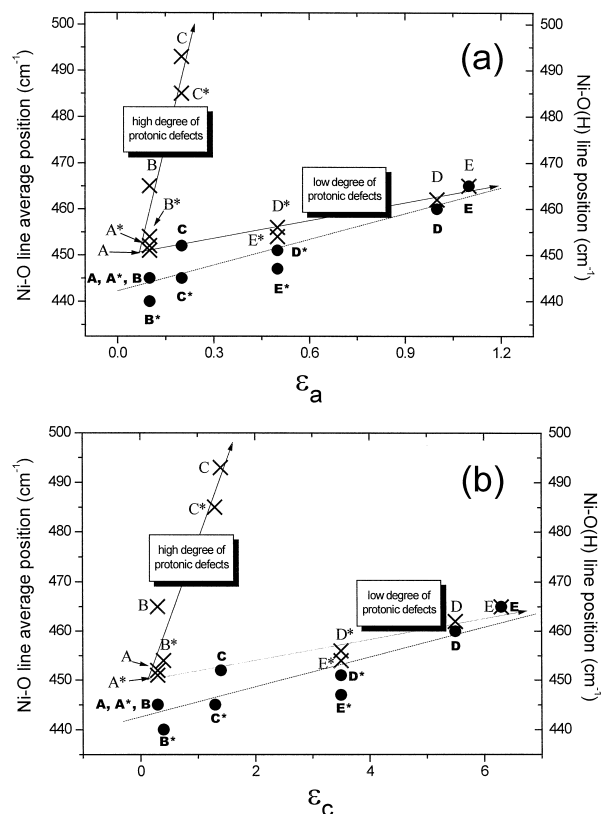
where ν_n is the frequency of the nth Ni–O peak and $A_{\nu n}$ is the area of the peak located at the ν_n frequency.

The double distribution obtained in Fig. 12 confirms that micro-strain cannot be solely attributed to the presence of proton vacancies and that its contribution is less important than other factors. Other structural defects, in addition to protonic defects, play a role in the crystalline distortion. An alternative source of lattice perturbations has to be examined, for example, the chemical adsorption of inorganic anions (carbonate and sulphate) at the border of the crystallites, whose presence is well established by IR spectroscopy in samples C–E and C*–E*.

5. Conclusions

The broadening of the diffraction bands cannot be assigned solely to the effect of the finite size of the diffraction coherent fields. The anisotropic behaviour of the diffraction peak broadening suggests the presence of micro-distortions in the lattice structure due to stacking faults, adsorption of inorganic species at the border of crystallites and also protonic vacancies which induce both isotropic and anisotropic broadening of Bragg reflections. The Rietveld refinement demonstrates the presence of micro-distortions in the structure as a result of micro-strain, which increases in the sequence of families $(hk0) \rightarrow (00l) \rightarrow (h0l)$. A high concentration of defects in the crystal lattice is correlated with the presence of high energy Ni–O bonds in the Raman spectra, which is unusual for a close-packed β-Ni(OH)$_2$. The presence of proton vacancies leads to a lower rate of distortion in the crystalline lattice than the stacking faults or the adsorption of inorganic species at the border of the crystallites. A smaller crystallite size is correlated with a greater rate of deformation in the crystalline lattice, especially for the peak dominated by the index l. This may suggest that an adsorption of molecular species onto the small crystallite edges could induce relevant perturbations.

After ageing in KOH (5N) solution for 5 days, an Ostwald ripening was found with convergence to a range of crystallite sizes ranging between 260 and 380 Å and a large decrease in the defect concentration.

Electrochemical tests are in progress to relate the degree of micro-strain to the electrochemical behaviour and to determine the efficiency of the nickel hydroxide produced by electrodialysis.

Acknowledgements

Appendix A. Rietveld refinement

In order to account for the anisotropic effects of size and micro-strain, we used the pseudo-Voigt Thompson–Cox–Hastings function to which additional terms have been added [31]. For the calculation of the anisotropic parameters of the micro-strain, a general function $\mathrm{DST}(\alpha, \iota, \gamma)$ was introduced to take account of the hexagonal symmetry of the network. For the anisotropic effect of size ($\mathbf{e} < \mathbf{d}$), a function FZ was introduced. The various contributions of the different parameters are summarized in Table 4.

The sample contribution to the peak broadening is of Lorentzian type, while the instrumental one gives a Gaussian character to the peak profiles. The relevant variables for a diffraction pattern are the $M_{hkl} = 1/d_{hkl}^2$. In the case of hexagonal symmetry, we have:

$$
\begin{aligned}
M_{hkl} &= 1/d_{hkl}^2 \\
&= 4/3a^2(h^2 + k^2 hk) + l^2/c^2 \\
&= Am^2 + Cl^2
\end{aligned}
\tag{4}
$$

where a and c are the cell parameters of the crystal lattice. In the presence of micro-strain, the peak profile is broadened by the constraint anisotropic term:

$$
\begin{aligned}
H^2 &= 8\ln(2)\left[\sigma^2(M_{hkl})/M_{hkl}^2\right]\tan^2(\theta) \\
&= \mathrm{DST}^2 \tan^2(\theta)
\end{aligned}
\tag{5}
$$

with

$$
\begin{aligned}
\sigma^2(M_{hkl}) &= \sigma^2 m^2 + (\iota^2 l^4) + 2(\alpha\iota\gamma m)l^2 \\
&= \alpha^2 m^2 + (\iota^2 l^4) + Qml^2
\end{aligned}
\tag{6}
$$

The term for broadening by micro-strain is made up of two components:

$$
\begin{aligned}
H^2 = \Big\{ &\left[\alpha^2 m^2/(Am^2 + Cl^2)\right] \\
&+ \left[l^2((\iota l)^2 + Qm)/(Am^2 + Cl^2)\right]\Big\}\tan^2(\theta)
\end{aligned}
\tag{7}
$$

The second term, which is the most important, becomes zero for $l = 0$. In fact, the lines with indices $(hk0)$ are

Table 4
Parameter contributions to the diffraction profile

	Isotropic		Anisotropic	
	Gaussian contribution	Lorentzian contribution	Gaussian contribution	Lorentzian contribution
Size effect	P	Y	–	FZ
Constraint effect	U	X	DST (α,ι,γ)	–

sharper. For example, the value $DST^2 = 8 \ln(2)\ c^2\iota$ calculated for (00l) is bigger than the value $DST^2 = 6 \ln(2)\ a^2\alpha$ calculated for (hk0) (see Table 5a and b).

By the Rietveld method, it is possible to refine the profile of diffractograms using as variables the peak positions and shapes. The total profile is analysed without any structure constraints, which implies a knowledge of the space group, but not of all the atomic positions. This method of refinement enables us to make a closer correlation with the peak-by-peak method, which does not take into account the structural parameters. The refinement of

B* and E* diagrams was carried out by keeping fixed the Caglioti factors obtained by the silica powder refinement (ν_O). The R_{wp} factors of reliability for the B* and E* compounds are 12.3% and 14.6%, respectively. Starting from the results obtained by the profile refinement, a total refinement was carried out using the crystallographic data deduced from the neutron diffraction study by Szytula et al. [32] on a polycrystalline β(II)-Ni(OH)$_2$ sample. The form profile parameters being fixed, only the positions, the occupancy rate and the thermal agitation factors were varied. The unconstraining of these parameters does not lead to an improvement in the convergence factors R_{Bragg}, equal to 9.6% and 14.6% for compounds B* and E*, respectively (Table 5a and b, model A). When the isotropic factors U, V, W are fixed, the refinement does not converge. Nevertheless, unconstraining both the form and crystallographic parameters leads to an appreciable improvement in the refinement (Figs. 5 and 6). The values of the parameters are reported in Table 5a and b, model B. The U, V, W determined for compound B* do not show too much variation when compared with those of silicon.

Table 5

(a) Profile and crystallographic parameters deduced from the refinement of sample B*

Profile						Crystallography						
						At.	Site	Location parameters			Occup	Agitation (Å²)
A												
U	V	W	P	X	Y			X	Y	Z		
0.0149	-0.01283	0.01351	0.01457	0	0.15039	Ni	1a	0	0	0	1	1
DST			FZ			O	2d	1/3	2/3	0.24	2	2
α	ι	γ	According to 101			H	2a	1/3	2/3	0.47	2	2
0.3809	1.1449	3.1586	1.2051									
Rwp = 21.9%, Chi2 = 3.57, RBragg = 9.58%												
B												
U	V	W	P	X	Y			X	Y	Z		B_{11} B_{22} B_{33} B_{12}
0.0311	0.02871	0.03460	0.05142	0	0.22169	Ni	1a	0	0	0	1	0.064 0.064 0.017 0.063
DST			FZ			O	2d	1/3	2/3	0.2266	2	1.6
α	ι	γ	According to 101			H	2a	1/3	2/3	0.4700	2	2.8
0.5662	1.0796	5.4734	0.84091									
Rwp = 15.8%, Chi2 = 1.85, RBragg = 6.43%												

(b) Profile and crystallographic parameters deduced from the refinement of sample E*

Profile						Crystallography						
						At.	Site	Location parameters			Occup	Agitation (Å²)
A												
U	V	W	P	X	Y			X	Y	Z		
0.0149	-0.01283	0.01351	0.38676	0	0.16121	Ni	1a	0	0	0	1	1
DST			FZ			O	2d	1/3	2/3	0.24	2	2
α	ι	γ	According to 001			H	2a	1/3	2/3	0.47	2	2
0.8663	4.7382	2.1626	0.36697									
Rwp = 24.8%, Chi2 = 2.36, RBragg = 14.6%												
B												
U	V	W	P	X	Y			X	Y	Z		B_{11} B_{22} B_{33} B_{12}
0.0724	-0.67971	0.56168	0.09024	0	0.29677	Ni	1a	0	0	0	1	0.102 0.102 0.075 0.102
DST			FZ			O	2d	1/3	2/3	0.2286	1.9876	0.051 0.051 -0.03 0.051
α	ι	γ	According to 001			H	2a	1/3	2/3	0.4788	1.8982	2
0.4385	4.6998	7.6883	0.366997									
Rwp = 20.2%, Chi2 = 1.53, RBragg = 10.2%												

References

[1] O.E.B. patent #0 559 590, 4 March 1993.

[2] P. Oliva, J. Leonardi, J.F. Laurent, C. Delmas, J.J. Braconnier, M. Figlarz, F. Fievet, A. de Guibert, J. Power Sources 8 (1982) 229.

[3] A. Delahaye-Vidal, B. Beaudoin, N. Sac-Epée, K. Tekaia-Elhsissen, A. Audemar, M. Figlarz, Solid State Ionics 84 (1996) 239.

[4] B.B. Ezhov, O.G. Malandin, Electrochemical Science and Technology 138 (1991) 885.

[5] C. Faure, Thesis, University Bordeaux I, 1990.

[6] A. Delahaye, Thesis, University of Picardie, 1986.

[7] M. Terasaka, M. Kanbayashi, T. Shiojidi, JP Patent No. 541213, 6 Aug. 1991.

[8] K. Watanabe, T. Kikuoka, N. Kumagai, J. Appl. Electrochem. 25 (1995) 219.

[9] R.Barnard, C.F. Randell, F.L. Tye, in J. Thompson (Ed.), Power Sources, Vol. 8, Academic Press, London, 1981, pp. 401–423.

[10] M.C. Bernard, R. Cortes, M. Keddam, H. Takenouti, P. Bernard, S. Senyarich, J. Power Sources 63 (1996) 247.

[11] C. Delmas, C. Tessier, J. Mater. Chem. 7 (8) (1997) 1439.

[12] P. Scherrer, Gött. Nachr. 2 (1918) 98.

[13] B.E. Warren, X-ray Diffraction, Addison-Wesley, Reading, MA, 1969.

[14] M.C. Bernard, M. Keddam, H. Takenouti, P. Bernard, S. Senyarich, J. Electrochem. Soc. 143 (1996) 2447.

[15] S.S. Mitra, Vibration spectra of solids, in: F. Seizt, D. Turnbull (Eds.), Solid State Physics 13 (1962) 1–80.

[16] L. Guerlou-Demourgues, C. Denage, C. Delmas, J. Power Sources 52 (1994) 269.

[17] L. Demourgues-Guerlou, J.J. Braconnier, C. Delmas, J. Solid State Chem. 104 (1993) 359.

[18] L. Demourgues-Guerlou, C. Delmas, J. Power Sources 45 (1993) 281.

[19] Y. Borthomieu, Thesis, University Bordeaux I, 1990.

[20] B.C. Cornilsen, P.J. Karjala, P.L. Loyselle, J. Power Sources 22 (1988) 351.

[21] B.C. Cornilsen, X. Shan, P.L. Loyselle, J. Power Sources 29 (1990) 453.

[22] R. Kostecki, F. McLarnon, J. Electrochem. Soc. 144 (1997) 485.

[23] A. Audemer, A. Delahaye, R. Farhi, N. Sac-Epée, J.-M. Tarascon, J. Electrochem. Soc. 8 (1997) 2614.

[24] A. Hasdou, G. Pourcelly, P. Huguet, J. Bribes, J. Sandeaux, C. Gavach, M. Dobouis, New J. Chem. 20 (1996) 515.

[25] P. Delichere, A. Hugot-Le Goff, N. Yu, J. Electrochem. Soc. 133 (1986) 2106.

[26] F. Fievet, M. Figlarz, J. Catal. 39 (1975) 350.

[27] C. Barriga, J.M. Fernandez, M.A. Ulibarri, F.M. Labajos, V. Rives, J. Solid State Chem. 124 (1996) 205.

[28] P. Vishnu Kamath, G. Helen Annal Therese, J. Gopalakrishnan, J. Solid State Chem. 128 (1997) 38.

[29] P. Genin, A. Delahaye-Vidal, F. Portemer, K. Tekaia-Elhsissen, M. Figlarz, Eur. J. Solid State Inorg. Chem. 28 (1991) 505.

[30] A. Delahaye-Vidal, K. Tekaia-Elhsissen, P. Genin, M. Figlarz, Eur. J. Solid State Inorg. Chem. 31 (1994) 823.

[31] J. Rodriguez-Carvajal, M.T. Fernandez-Diaz, J.L. Martinez, J. Phys.: Condens. Matter 3 (1991) 3215.

[32] A. Szytula, A. Murazaki, M. Balanda, Phys. Status Solidi B 43 (1971) 125.